# Isochrone fitting to the open cluster M67 in the era of Gaia and improved model physics

Claudia Reyes[1], Dennis Stello[2,1], Marc Hon[3,4], Regner Trampedach[5], Eric Sandquist[6], and Marc H. Pinsonneault[7].

[1]*School of Physics, University of New South Wales, NSW 2052, Australia*
[2]*Sydney Institute for Astronomy (SIfA), School of Physics, University of Sydney, NSW 2006, Australia*
[3] *Department of Physics and Kavli Institute for Astrophysics and Space Research, Massachusetts Institute of Technology, 77 Massachusetts Ave, Cambridge, MA 02139, USA.*
[4]*Institute for Astronomy, University of Hawaii, 2680 Woodlawn Drive, Honolulu, HI 96822, USA*
[5]*Space Science Institute, 4765 Walnut Street, Boulder, CO 80301, USA*
[6]*Department of Astronomy, San Diego State University, San Diego, CA 92182, USA*
[7]*Department of Astronomy, The Ohio State University, Columbus, OH 43210, USA*

Accepted XXX. Received YYY; in original form ZZZ

**ABSTRACT**

The Gaia mission has provided highly accurate observations that have significantly reduced the scatter in the colour-magnitude diagrams of open clusters. As a result of the improved isochrone sequence of the open cluster M67, we have created new stellar models that avoid commonly used simplifications in 1D stellar modelling, such as mass-independent core overshooting and a constant mixing length parameter. This has enabled us to deliver a precise isochrone specifically designed for M67, available for download. We follow a commonly-used qualitative approach to adjust the input physics to match the well-defined colour-magnitude sequence, and we test the model-predicted masses against a known eclipsing binary system at the main sequence turnoff of the cluster. Despite using improvements in photometry and stellar physics we cannot match the masses of both binary components with the same theoretical isochrone. A $\chi^2$-based isochrone fitting approach using our preferred input physics results in a cluster age of $3.95^{+0.16}_{-0.15}$ Gyrs.

**Key words:** Hertzsprung–Russell and colour–magnitude diagrams – open clusters and associations: individual: M67

## 1 INTRODUCTION

The old open cluster M67 (NGC 2682) is known to be an important testbed for stellar evolution studies because of its low reddening, near-solar metallicity, and rich stellar population. Its turnoff stars fall right in the mass range where we can infer how convective core size depend on stellar mass, making M67 particularly challenging, but also one of the only sites where we can use the colour-magnitude diagram to map out the convective core effects so readily. The colour-magnitude diagram of M67, together with stellar models, has therefore been used to determine the extent of convective core overshooting, to calibrate colour-temperature relations, and to test solar abundances. Examples include VandenBerg & Stetson (2004) and VandenBerg et al. (2007) who used *BV* photometry from Montgomery et al. (1993) and later Magic et al. (2010) who used the higher precision *BV* photometry from Sandquist (2004).

An unusually large fraction of binaries and blue stragglers have been revealed through the study of M67's colour-magnitude diagram (Strom et al. 1971; Mathieu & Latham 1986; Mathys 1991; Gilliland et al. 1993; Mathieu et al. 2003), and through spectroscopy (Geller et al. 2015; Leiner et al. 2019; Geller et al. 2021). Various spectroscopic studies have also focused on the chemical abundances of M67 and have reported the signature of diffusion processes in the cluster's stars (Souto et al. 2018; Bertelli Motta et al. 2018; Souto et al. 2019; Liu et al. 2019; Beeson et al. 2024). In addition, the cluster's giants have been the targets of asteroseismic studies with both ground-based (Gilliland et al. 1993; Stello et al. 2006) and space-based telescopes (Stello et al. 2016; Li et al. 2024).

Since the first release of data from the Gaia mission (Gaia Collaboration et al. 2016), the observed colour-magnitude diagrams of clusters like M67 became significantly less scattered, and as a result new efforts to match theoretical isochrones to clusters have been made, including to M67 (Gaia Collaboration et al. (2018b); Choi et al. (2018); Nguyen et al. (2022)). However, none of the existing Gaia-era isochrones were explicitly created for M67 as the end goal, and as a result they do not match the Gaia data particularly well (Appendix B, Figure B1). Furthermore, they use the common approach of adopting a fixed mixing length parameter, $\alpha_{\rm MLT}$, usually calibrated to the Sun, although there is no strong evidence suggesting $\alpha_{\rm MLT}$ is the same for stars of different evolutionary stages (Song et al. 2020). This simplification can be expected to influence the temperatures and luminosities of stars with convective envelopes (Joyce & Tayar 2023).

In this paper, we aim to develop a new theoretical isochrone that incorporates the latest research on the physics governing stellar evolution: notably, model improvements based on hydrodynamical 3D

simulations of convection (Trampedach et al. 2014a,b) while improving the fit to the colour-magnitude diagram. Such isochrone, validated by Gaia's M67 data, will provide an isochrone reference for future studies. Additionally, we address the issue of the eclipsing binary WOCS11028, whose stellar components have highly accurate determinations of mass and radius and are found to likely not have interacted in the past (See Sandquist et al. 2021, for an extensive discussion). The problem is that no existing isochrone models simultaneously match these properties for both components.

Our approach is as follows: we begin using a traditional qualitative isochrone fitting approach (VandenBerg & Stetson 2004; Pinsonneault et al. 2004; Barker & Paust 2018) for empirical calibration of the input physics. Lastly, inspired by Li et al. (2023), who explored a two-parameter grid to estimate age and extinction likelihoods in NGC 2516, we estimate age and distance modulus likelihoods for our models given our preferred input physics using a $\chi^2$ approach.

## 2 THE M67 COLOUR-MAGNITUDE DIAGRAM

### 2.1 Membership sample

We determined cluster membership using Gaia DR3 (Gaia Collaboration 2022) from stars within 2 degrees of the centre of the cluster at RA = 132.85°, Dec = 11.81° (Figure 1a), selecting the overdensity of stars with radial velocities within $34 \pm 13.6$ km/s and parallax $1.15 \pm 0.12$ mas (Figure 1b), and proper motions within 0.7 mas/year from $\mu_\alpha = -11.0$ mas/year and $\mu_\delta = -2.9$ mas/year in the proper-motion space (Figure 1c). To boost the number of stars along the less populated giant branch, we further added ten giant stars with secure kinematic membership from ground-based radial velocities by Geller et al. (2015) that: (1) did not have DR3 radial velocities available (white circles in Figures 1a and 1c), or (2) narrowly missed our Gaia-based cuts in parallax or proper motion (orange and/or yellow circles in Figure 1), but were later confirmed by colour-magnitude diagram position to belong to the cluster's standard-evolution single-star sequence. In total, our selection resulted in 488 cluster members: 22 non-standard evolution stars such as blue stragglers, yellow giants, and sub-subgiants; 361 main sequence stars, 63 subgiants, 35 red giant branch stars, and 7 red clump stars. This number includes four new stars that were not identified by Geller et al. (2015) as M67 members, but met all of our selection criteria for cluster membership, as shown in Figure 2 with yellow squared symbols. Table 1 lists the stars mentioned above, along with their corresponding IDs from various catalogues.

### 2.2 Observed Colour-Magnitude Diagram

#### 2.2.1 Photometry

We compared M67 photometry from Gaia DR2 (Gaia Collaboration et al. 2018a) and DR3 (Gaia Collaboration 2022) and found a similar scatter in the colour-magnitude sequence of the two systems. Therefore, either system could be used for isochrone fitting without precision loss. We decided to use Gaia DR2 because the deconvolution photometry of the eclipsing binary WOCS 11028 (Sandquist et al. 2021) at the cluster's turnoff is not directly available in Gaia DR3 magnitudes, and we want to use the binary system during the isochrone fitting (section 3).

#### 2.2.2 Isochrone fitting sample

We exclude from our isochrone-fitting sample those stars identified as binary, likely binary, stragglers, or possibly contaminated by a nearby source according to Geller et al. (2015), and stars from the Gaia DR3 non-single star catalogue Gaia Collaboration et al. (2022). Following Khan et al. (2019), we also remove stars with a renormalised unit weight error (RUWE) that exceeds 1.2 in DR2, all of which are likely to fall far from the tight single-star cluster sequence in the colour-magnitude diagram. This selection results in a sample of 369 stars (small grey and black dots in Figure 3). The confidence level that this sample is free of multiple star systems mainly depends on the accuracy of the radial velocities from Geller et al. (2015), which degrade toward stars fainter than $12^{\text{th}}$ magnitude in $V$ (see their Figure 4). To take care of the remaining stars that clearly belong to the binary main sequence by their position in the colour-magnitude diagram, we made a further manual cut that brings the isochrone fitting sample to the 309 stars shown in black in Figure 3.

#### 2.2.3 Reddening

For differential de-reddening of the photometry, we sought the latest version of the Bayestar 3D dust maps (Green et al. 2019). However, we found that these maps lacked resolution and did not behave smoothly in the direction of M67 (See Appendix C). Thus, we performed de-reddening on a star-by-star basis using 2D dust maps by Planck Collaboration et al. (2016), and calculated individual extinction coefficients using the formulae from Danielski et al. (2018) with polynomial coefficients as calculated by Gaia Collaboration et al. (2018b) assuming $R_V = 3.1$. The averages of the full membership sample of 488 stars are $E(BP - RP) = 0.059 \pm 0.007$ and $A_G = 0.104 \pm 0.012$ magnitudes. Assuming $E(B - V) = 0.041$ as in Taylor (2007), our values are in agreement with Stassun et al. (2019) who found the relations $E(BP - RP) = 1.31 \cdot E(B - V)$ and $A_G = 2.72 \cdot E(B - V)$. Even in a low reddening cluster like M67, applying individual corrections for dereddening and extinction reduced the scatter of the colour-magnitude sequence. This was most noticeable around the hook and the lower red giant branch, but also along the main sequence (compare Figures 3a and b).

#### 2.2.4 Distance

We derived the distance modulus from our sample using Gaia DR3 parallaxes, which are shown to have increased precision by 30% over DR2 parallaxes (Gaia Collaboration et al. 2021), and we applied zero point offsets calculated for each star following Lindegren et al. (2021), who found that zero-points depend on stellar magnitude, colour, and ecliptic latitude. The mean zero-point corrected parallax derived this way is $\bar{\omega} = 1.195 \pm 0.027$ mas corresponding to a distance modulus $= 9.614 \pm 0.049$ magnitudes. This is a smaller distance modulus than the values of 9.726 and 9.730, derived by Gaia Collaboration et al. (2018b) and Choi et al. (2018), respectively, and also smaller than 9.690 adopted by Nguyen et al. (2022), but close to 9.630 by Sandquist et al. (2021). These four studies base their distance modulus calculation on Gaia DR2 parallaxes, but the latter two apply a parallax zero-point offset. Nguyen et al. (2022) correct their value applying directly the offset of $-30\mu$as found by Lindegren et al. (2018), while Sandquist et al. (2021) estimate an offset of $-54\mu$as considering the results by Stassun & Torres (2018), Zinn et al. (2019), and Schönrich et al. (2019) in addition to Lindegren et al. (2018).

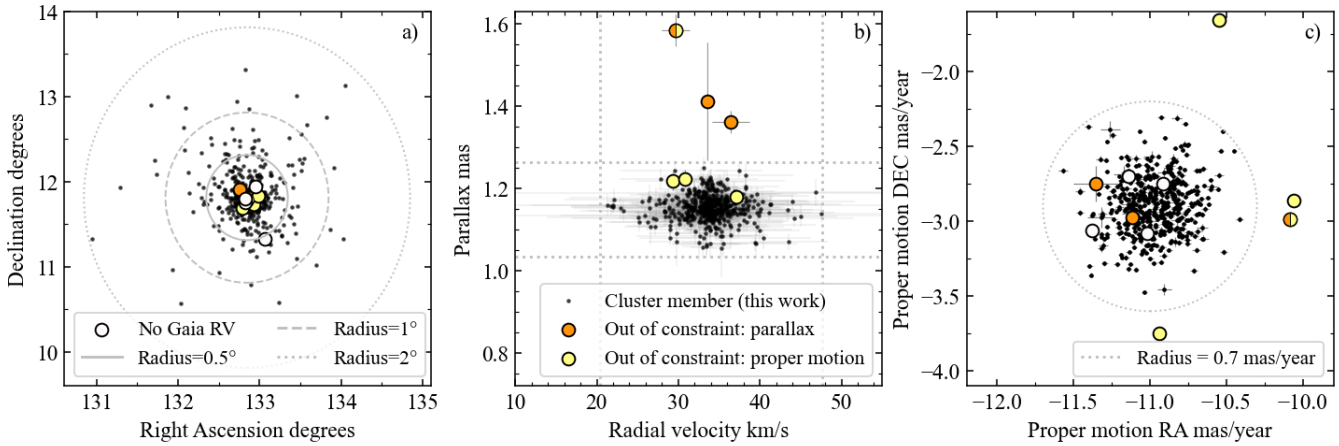


**Figure 1.** In small black symbols are cluster members as per our selection using DR3 values. Large circles are the ten stars we added because they were deemed cluster members by Geller et al. (2015) despite not being in our Gaia-based selection. Of those: (1) white circles show stars with no Gaia DR3 radial velocities available, (2) orange circles are stars that missed our cut in parallax, and (3) yellow circles are those outside our proper motion cut. The star shown in half-orange and half-yellow, WOCS 7004, falls outside of our proper motion and parallax cuts.

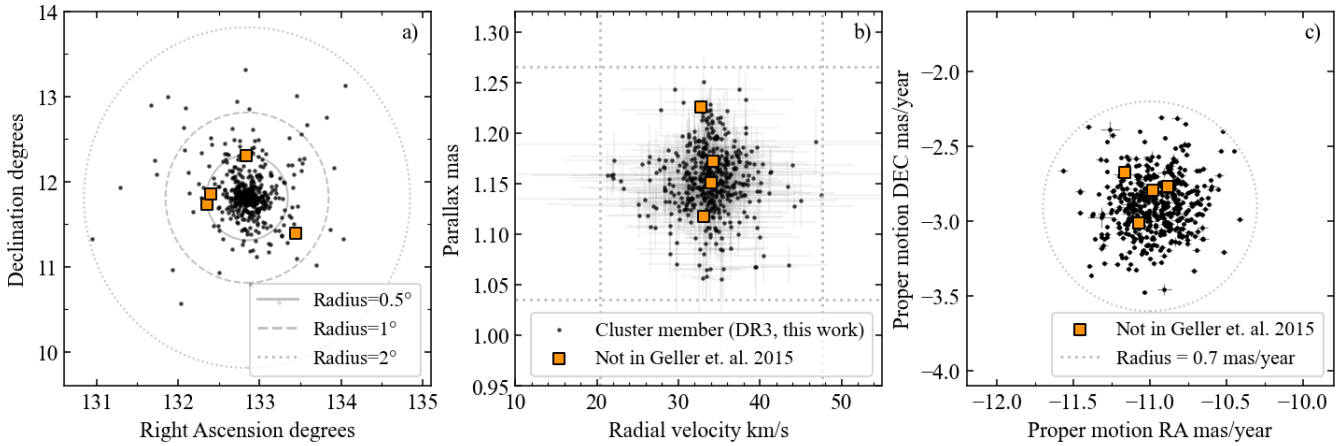


**Figure 2.** The three panels show stars considered cluster members according to our Gaia-based selection. Stars in black symbols are also part of the membership sample by Geller et al. (2015), while orange squares show the four red giant stars that were not considered cluster members by Geller et al. (2015).

| Sanders[1] | WOCS[2] | EPIC[3] | Gaia DR3[4] | In DR3 selection | Geller'15 member | Comment |
|---|---|---|---|---|---|---|
| S 1016 | 2004 | 211410817 | 604917594995372544 | No | Yes | No RV available |
| S 978 | 1008 | 211407537 | 604911375882674560 | No | Yes | No RV available |
| S 1319 | 5021 | 211420451 | 604923470510324224 | No | Yes | No RV available |
| S 1557 | 1065 | 211380313 | 604696730596495744 | No | Yes | No RV available |
| S 1264 | 3004 | 211411629 | 604917835513458688 | No | Yes | Missed cuts in Parallax |
| S 806 | 5016 | 211417812 | 604969061587592064 | No | Yes | Missed cuts in Parallax |
| S 1221 | 2014 | 211406541 | 604904503934969856 | No | Yes | Missed cuts in Proper Motion |
| S 961 | 2017 | 211403555 | 604910001493155584 | No | Yes | Missed cuts in Proper Motion |
| S 1463 | 4017 | 211413064 | 604918522708195584 | No | Yes | Missed cuts in Proper Motion |
| S 1000 | 7004 | 211409644 | 604917320117398528 | No | Yes | Missed cuts in PLX + PM |
| S 258 | 1054 | 211414351 | 604965664269158656 | Yes | No | Red Giant, single star |
| S 1135 | 2059 | 211443624 | 605015309794935552 | Yes | No | Red Giant, single star |
| S 247 | 5059 | 211406144 | 598959032246073216 | Yes | No | Red Giant, binary star |
| S 2000 | - | 211384259 | 604689308892956416 | Yes | No | Red Giant, No WOCS ID |

[1]Sanders (1977), [2]Yadav et al. (2008), [3]Huber et al. (2017), [4]Gaia Collaboration (2022)

**Table 1.** The 10 stars from Figure 1 and the 4 stars from Figure 2, along with their commonly used names.

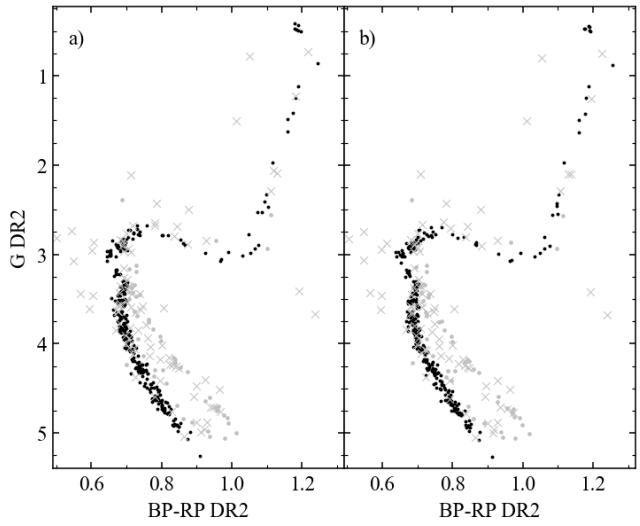


**Figure 3.** Black symbols represent stars in the isochrone fitting sample, grey 'x' symbols show presumed binaries or presumed products on non-standard evolution, and grey points show stars we later removed from the isochrone-fitting sample (see Section 2.2.2) (a) M67 colour-magnitude diagram (absolute magnitudes) after uniform reddening (2.72 x 0.041 G-magnitudes) and extinction (0.06 BP-RP magnitudes) corrections. (b) Applying differential corrections based on dustmaps and stellar coordinates.

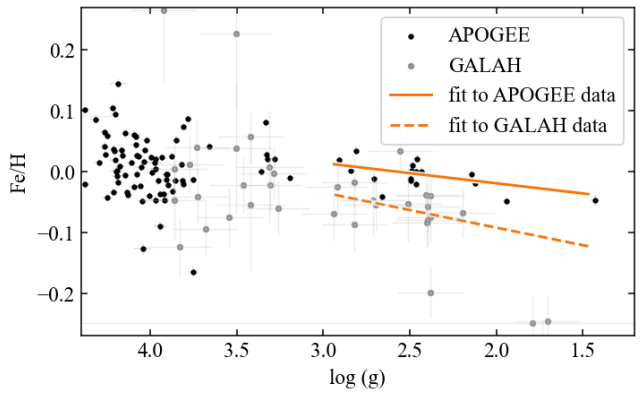


**Figure 4.** Metallicities and $\log(g)$ by APOGEE DR17 and GALAH DR3 for stars overlapping with our 488 cluster members. The orange lines show fits to the metallicities of the stars with $\log(g) < 3.0$ for both APOGEE (solid line) and GALAH (dashed line). In the latter, two extreme outliers at low $\log(g)$ and low [Fe/H] were excluded from the fit. All but one of the stars in the GALAH sample are also in the APOGEE sample

.

### 2.2.5 *Metallicity*

M67 has been observed extensively by spectroscopic surveys and it has even been used as a calibration cluster for APOGEE (Spoo et al. 2022). Naturally, we turned to this survey for updated M67 metallicity values. Figure 4 shows [Fe/H] from APOGEE DR17 for our cluster members (black dots). We noticed a decreasing metallicity trend with decreasing $\log(g)$, affecting the sample's most evolved giants. This was also observed in other open clusters from DR17 (See Appendix D). For comparison, we looked at GALAH DR3 results of M67 (grey dots) (Buder et al. 2021). Even though the GALAH data has higher dispersion and uncertainties, it also showed a descending trend with $\log(g)$, albeit more pronounced. This common trend is likely systematics from not using a full 3D-NLTE approach in the spectroscopic analysis, affecting stars with $\log(g) \approx$ 3-2.5 or lower. No physical mechanism intrinsic to the stars can explain such metallicity decline in stars undergoing convective mixing in the atmosphere. This issue could lead to an error in [Fe/H] of up to 1 dex in some cases (for example, NGC 2632 in Figure D1). Therefore, we caution against relying on giant star metallicities from non-3D-NLTE spectroscopic results, and we turn to recent M67 literature to find an appropriate [Fe/H] value for our models.

The average metallicity across all SDSS DR12 (Alam et al. 2015) M67 observations was reported as [Fe/H] = 0.08 ± 0.03 by Stello et al. (2016), with solar reference from Asplund et al. (2005). Two recent studies have used high-resolution spectroscopic observations to examine the chemical abundance trends of stars along the cluster isochrone to investigate the effects of atomic diffusion. Liu et al. (2019) used Keck/HIRES spectra to obtain high-precision atmospheric parameters and elemental abundances, and Souto et al. (2019) based their work on APOGEE DR14 data (Holtzman et al. 2018). They both found that stellar models needed to have a [Fe/H] between 0.0 and 0.1 to match the detailed chemical abundance patterns, and both used MIST tracks with diffusion (Choi et al. 2016), and the solar mixture by Asplund et al. (2009) (the AGSS09 scale). Souto et al. (2019) found no significant abundance difference in M67 stars of the same evolutionary class, but found abundance differences between stars in different evolutionary stages of up to ~ 0.5dex. They found that the observed abundance trends can be explained by diffusion processes, and estimated a reduction in the efficiency of gravitational settling of 15%.

## 3 ISOCHRONE MODELS

We produce custom isochrones tailored to M67 using MESA version 23.05.1 (Paxton et al. 2011, 2013, 2015, 2018, 2019; Jermyn et al. 2023). To transform the theoretical isochrones into magnitudes that allow for direct comparisons with observations, we use bolometric correction tables from the MIST project[5], which are based on the grid of stellar atmospheres and synthetic spectra described by Choi et al. (2016). Our approach for selecting model parameters to match M67, resulting in our final preferred isochrone, named Isochrone A[6], is described in the following. Table 2 summarises Isochrone A's parameters.

### 3.1 Initial chemical composition

Guided by the results detailed in 2.2.5 we decided to adopt the AGSS09 scale, [Fe/H] = 0.05, and $Z = 0.016$, implying a helium enrichment law of $\Delta Y/\Delta Z = 1.2$ when primordial helium is taken as $Y_p = 0.248$. While helium is not solar-scaled, similar values of $\Delta Y/\Delta Z$ have been used to match models to data in other open clusters: 1.4 was found for NGC 6791 (Brogaard et al. 2012), 1.2 for the Hyades (Brogaard et al. 2021), and an average of 1.25 for NGC 6811 (Sandquist et al. 2016). Souto et al. (2019) predicted [Fe/H] ~ 0.05 (our chosen primordial metallicity) for M67 solar analogues using

[5] https://waps.cfa.harvard.edu/MIST/model_grids.html
[6] Isochrone A and Inlists available on Zenodo https://zenodo.org/records/12616441

| Parameter | Isochrone A |
|---|---|
| Age | 3.95 Gyrs |
| Distance modulus | 9.614 |
| Nuclear reaction network | h1, he3, he4, c12, n14, o16, ne20, mg24 (MESA's basic.net) |
| Solar mixture | AGSS09 (Asplund et al. 2009) |
| Z | 0.016 |
| Y | 0.267 |
| $\Delta Z/\Delta Y$ | 1.2 |
| EoS | HELM (Timmes & Swesty 2000) + Skye (Jermyn et al. 2021) + FreeEOS (Irwin 2004) + OPAL (Rogers & Nayfonov 2002) + SCVH (Saumon et al. 1995) |
| Interior opacities | OPAL (Iglesias & Rogers 1993, 1996) |
| Opacities | AESOPUS (Marigo & Aringer 2009) |
| Atmospheres | T($\tau$), varying, Trampedach solar (Trampedach et al. 2014a; Ball 2021) |
| Overshooting | Exponential, increasing with mass. |
| $\alpha_{\rm MLT}$ | Varying with $T_{\rm eff}$ and $\log(g)$, follows 3D grid (Trampedach et al. 2014b) |
| Scaling factor $k_{\alpha_{\rm MLT}}$ | 1.11 |
| Mass loss | No |
| MLT_option | Henyey |
| Convection | Schwarzschild criterion |
| Diffusion | Yes |

**Table 2.** Summary of parameters in MESA models for the isochrone shown in Figure 7. The isochrone is presented in A1

.

their estimated diffusion factor, which is consistent with our models if we consider our lower than solar initial helium, and their solar scaled models.

Our choice of $Z$ achieves good colour agreement with the main sequence for ages within the range quoted in literature: 3.5 - 4.3 Gyrs (VandenBerg & Stetson 2004; Sarajedini et al. 2009; Barnes et al. 2016), while the chosen helium content, $Y = 0.267$, results in slightly more massive stars for a given luminosity compared to solar-scaled models. This becomes relevant when taking into account the eclipsing binary WOCS 11028 (Section 3.6).

### 3.2 Model atmospheres

One-dimensional stellar evolution codes like MESA include simplifications in their representation of the outer layers of a star, such as using a single and fixed value of the convective mixing length $\alpha_{\rm MLT}$, which is commonly anchored to the Sun. In our models, we seek to incorporate more realistic values of $\alpha_{\rm MLT}$. This, we take from interpolations to the grid of hydrodynamical 3D simulations of stellar convection – the 3D grid – by Trampedach et al. (2014b) evaluated at every step according to $\log(g)$ and $T_{\rm eff}$ with a scaling factor $k_{\alpha_{\rm MLT}}$, following Mosumgaard et al. (2018), except that we calibrate $k_{\alpha_{\rm MLT}}$ to M67 rather than to the Sun (Section 3.5.1).

To ensure the correct photospheric transition to the outer part of the models, we follow the formulation of generalised Hop-functions for atmospheres by Trampedach et al. (2014a) from 3D simulations of convection in deep stellar atmospheres: ($T(\tau)$=`Trampedach_solar`) as implemented by Ball (2021), and we modify the radiative gradient so that regions of low optical depth have a temperature that follows this $T(\tau)$ relation. The results of applying the improvements described above to a base form of Isochrone A can be observed in Appendix B, by comparing Figures B2a and b.

While studying the effects of varying model parameters, we saw that the selection of low-temperature opacities had a significant impact on the temperatures and luminosities of the models. As a result, we have opted to use low-temperature opacities from the AESOPUS (Accurate Equation of State and Opacity Utility Software) tables because the AESOPUS code (Marigo & Aringer 2009) accounts for the processing of CNO in giant stars while the MESA default tables FA05 (Ferguson et al. 2005) do not. The effect of additionally changing from FA05 to AESOPUS opacity tables can be observed in Appendix B, by comparing Figures B2b and c.

### 3.3 Overshooting

We implement exponential diffusive overshoot (Herwig 2000) at the Hydrogen core with a strength set to increase gradually with mass, following the expression proposed by VandenBerg et al. (2006):

$$f_{\rm ov} = f\left[1 - \cos\left(\pi \frac{M_\star - M_{\rm full\_off}}{M_{\rm full\_on} - M_{\rm full\_off}}\right)\right] \quad (1)$$

where $M_*$ is the mass along the isochrone, $M_{\rm full\_off} = 1.10\,{\rm M}_\odot$, $M_{\rm full\_on} = 1.80\,{\rm M}_\odot$, which provides a smooth transition between 0 and $f_{\rm ov}$. We set the parameter $f_0$ as $f_{\rm ov}/2$, where $f_0$ is a distance from the edge of the convective zone where the diffusion mixing coefficient is measured. This coefficient is then multiplied by $e^{-2z/f_{\rm ov}Hp}$, where $Hp$ is the pressure scale height, so that the mixing efficiency declines exponentially into the radiative zone with distance $z$ from the convective boundary.

While it is common to define overshoot in terms of $Hp$, this poses a problem when $f_{\rm ov}$ is kept fixed for all masses because $Hp \to \infty$ when the convective core radius $\to 0$. By default, MESA limits $f_{\rm ov}Hp$ to the size of the convective zone, however, this could still result in unphysically large convective cores in low mass stars, as, according to Roxburgh (1992) overshooting should not expand the convective core more than 18% of its 'no-overshoot' size. A mass-dependent overshoot like the one from Equation (1) helps overcome this problem. Another common criterion that avoids the issue is to express the overshoot extent as a fraction of the core radius. The effect of the change from a fixed overshoot to our adopted mass-dependent values can be seen in Appendix B, by comparing the black and green curves in Figure B2c.

### 3.4 Mass Loss

We do not have a complete understanding of the mass-loss processes operating during the red giant phase (Karakas 2017). Choi et al. (2016) selected a Reimers parameter $\eta = 0.1$ for use in their MIST models based on the initial-final mass relation in the Magellanic Clouds. Miglio et al. (2012) found from asteroseismology that the mass difference between red giant branch and red clump stars of the metal-rich open cluster NGC 6791 can be described with a Reimers parameter in the range $0.1 < \eta < 0.3$, lower than predicted by the commonly used prescription by Reimers (1975). They also found that the near-solar-metallicity open cluster NGC 6819 is compatible with no mass loss. Stello et al. (2016) measured the masses of M67 giants using asteroseismology and found no significant mass difference between the red clump and the red giant branch. Considering all these results, and especially the evidence from M67 asteroseismology, we decided to run models without mass loss. Regardless, mass loss is unlikely to significantly affect our M67 isochrone fit because nearly all mass loss occurs at the very end of the red giant branch, and red clump stars will be excluded from the final fit (see Section 4).

### 3.5 Empirical Calibrations

Bringing together our model prescriptions as described above and the extinction-corrected M67 colour-magnitude diagram from Section 2.2, we can now fine-tune the mixing length and overshooting.

#### 3.5.1 Mixing Length Parameter

Figure 5a shows Isochrone A colour-coded by our adopted mixing length, resulting from applying the scaling factor $k_{\alpha_{\rm MLT}} = 1.11$ to the 3D grid. Because the 3D grid stops below $\log(g)$ ~2.4 –segmented line in Figure 5b–, we keep the last interpolated grid value for the rest of the evolution up the giant branch, but doing so puts the isochrone's red clump at lower temperatures than observed from the cluster's clump stars. To resolve this issue, we decided to set $\alpha_{\rm MLT}$ to 1.93 after the helium flash, which makes Isochrone A agree with the observations of the red clump. However, this does not necessarily mean that 1.93 is the correct mixing length value for stars with $T_{\rm eff}$ and $\log(g)$ similar to the M67 clump stars. It merely expresses our ignorance of the behaviour of $\alpha_{\rm MLT}$ after the 3D grid stops and also compensates for other shortcomings that our helium core burning models might have that would affect $T_{\rm eff}$.

#### 3.5.2 Overshooting

The effect of the overshooting parameter is seen primarily near the isochrone's turnoff due to the turnoff's sensitivity to the size of the convective core and how the size of the convective core depends on stellar mass. Figures 5c and d show Isochrone A colour-coded by $f_{\rm ov}$ and stellar mass, respectively. Figure 6 shows our mass-dependent overshooting parameter $f_{\rm ov}$, compared to the reported $f_{\rm ov}$ by Claret & Torres (2017, 2018) in orange symbols, where models using exponential overshooting with diffusion are fitted to eclipsing binary masses.

There have been several recent studies on overshooting, but they often use different methods that cannot be directly compared to our calibration. For example, Lindsay et al. (2024) applies 'step' overshoot instead of exponential, and maintains a fixed value of $f_0$ while they vary $f_{\rm ov}$ and take care of the issue of large cores at low masses mentioned in Section 3.3 by switching from units of $Hp$ to units of core radius if $Hp$ is larger than the core radius. For an in-depth review of their results in the context of results from various overshooting studies, including Claret & Torres (2017, 2018), we refer the reader to Lindsay et al. (2024).

### 3.6 Eclipsing Binary WOCS 11028

The discovery of the eclipsing binary WOCS 11028 (Sandquist et al. 2021), with one component near the cluster turnoff, provides an opportunity to test how well stellar models can describe the cluster. Sandquist et al. (2021) found discrepancies of at least 0.17 mag ($\sim 10\sigma$) between the absolute magnitude of the primary component of the binary system and predictions by various stellar evolution codes, or equivalently a lower than predicted mass by $\delta m = 0.05 M_{\odot}$, even for isochrones as young as 3.2 Gyr. Nguyen et al. (2022) with their updated PARSEC isochrones report similar discrepancies.

Our Isochrone A-predicted G-magnitudes for the eclipsing primary and secondary (Figure 7, inset) are respectively, $+0.21 \pm 0.06$ and $-0.05 \pm 0.09$ magnitudes relative to the eclipsing binary estimates in Table 3. This includes uncertainties from our distance modulus and from the magnitudes and masses of the eclipsing binary. These offsets are comparable to the ones obtained by Sandquist et al. (2021) and Nguyen et al. (2022). Like us, Nguyen et al. (2022) found isochrones that agreed with the secondary within uncertainties but not with the primary. This is concerning because Sandquist et al. (2021) reported lower confidence in estimating the secondary star's magnitude compared to the primary.

#### 3.6.1 Alternative Isochrone EB

To address the eclipsing binary issue, we attempted to anchor an alternative isochrone on the mass and magnitude of the primary (WOCS 11028a) within $1\sigma$, as shown in the inset of Figure 8. To match the mass of the primary, we needed an isochrone with a main-sequence absolute brightness that is 0.2 magnitudes fainter compared to Isochrone A for a given mass. This can be achieved by making specific parameter adjustments, such as lowering the helium content, changing the reference element mixture, reducing isochrone age, increasing the distance modulus, or adding more reddening. Although all modifications will also move the secondary, applying one or more of these modifications could reconcile discrepancies with the primary, but it may also result in inconsistencies in other parts of the isochrone. For instance, a lower isochrone age leads to a subgiant branch morphology that does not match the M67 observed data, but that, in turn, could be resolved with increased shell overshoot values. Considering the above, we developed a few alternative isochrones that could be anchored on WOCS 11028a. None of them, however, could match both binary components simultaneously, and all of them violated at least one other constraint. We consider that some constraints are more reliably established than others. The cluster's reddening has been consistently measured at $E(B-V) = 0.04 \pm 0.04$ magnitudes, or its equivalent in other bands (Nissen et al. 1987; Schlegel et al. 1998; Taylor 2007), which agrees with our calculations from Planck Collaboration et al. (2016) dust maps. Additionally, the helium content should not be much lower than the Sun's, given the near-solar age and metallicity of the cluster, and it should certainly be higher than the primordial helium abundance. In contrast, historical discrepancies in the parallax measurements for M67 exist (see Section 2.2.4), and convective overshoot is known to be a significant source of uncertainty in stellar models (Kippenhahn et al. 2013; Salaris & Cassisi 2017; Viani & Basu 2020). Therefore, we present here our best-fit alternative model, Isochrone EB, which varies these less-established constraints. We achieve a good match between Isochrone EB and the data by using: (a) the solar mixture from Grevesse & Sauval (1998) with initial $Z = 0.0196$, $Y = 0.2710$ ($\Delta Y/\Delta Z = 1.18$), (b) a distance modulus of 9.73, $2.4\sigma$ larger than our derived value from zero-point corrected Gaia DR3 parallaxes, (c) and a sharp and significant increase in overshoot at and beyond $1.32\,M_{\odot}$, with manually adjusted values of $\alpha_{\rm MLT}$. The model parameters of Isochrone EB are summarised in Table 4, and a comparison of its overshoot and mixing length to those of Isocrone A are shown in Figures 9a and b, respectively.

We note that in Isochrone EB (Figure 9a), the values of overshooting in stars more massive than $1.35 M_{\odot}$ make the models exceed the upper limit given by the Roxburgh criterion for small convective cores, where overshooting is limited to a level that would prevent the core from growing to more than 18% of its 'no-overshoot' size (Roxburgh 1992). Furthermore, the study of convective overshooting remains a very active field, with various stellar signatures being used to calibrate models in different studies. Still, all recent studies find either a gradual increase with mass (Lindsay et al. 2024) or no increase at all (Constantino & Baraffe 2018).

From Figure 9b, we see some correspondence between the shapes described by both $\alpha_{\rm MLT}$ curves if we consider that the masses of

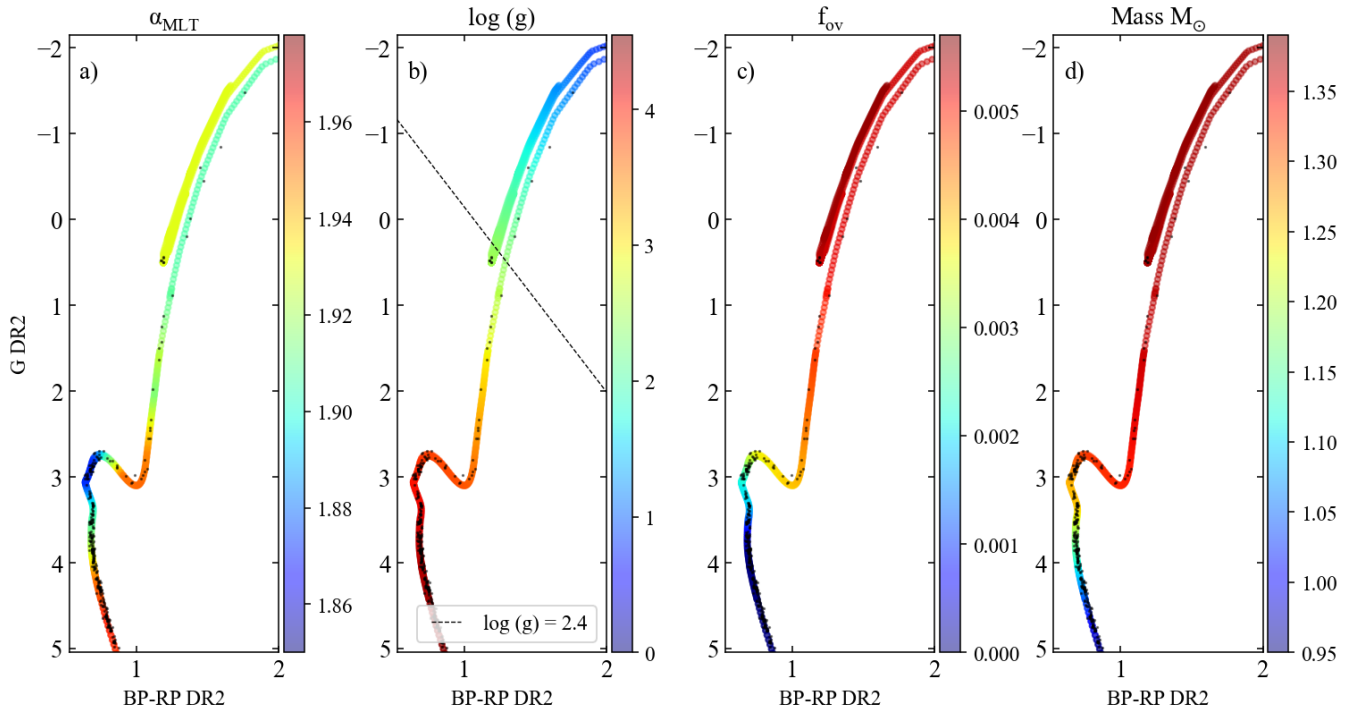


**Figure 5.** Isochrone A and M67 presumed single stars in absolute magnitude and colour-coded by (a) $\alpha_{\rm MLT}$, (b) $\log(g)$, (c) overshooting parameter $f_{\rm ov}$, and (d) stellar mass. The dashed line in b) crosses the isochrone where the $\alpha_{\rm MLT}$ 3D grid stops at $\log(g)$ 2.4. After that point in the evolution up the RGB, we set our models to maintain the last measured $\alpha_{\rm MLT}$ value and after helium ignition $\alpha_{\rm MLT}$ is set to 1.93.

| Binary Member | BP-RP* | $G^*$ | $2\sigma$(G) | Mass $M_\odot$ | Radius $R_\odot$ |
|---|---|---|---|---|---|
| WOCS 11028a | 0.686 | 13.336 | 0.035 | 1.222 ± 0.006 | 1.430 ± 0.030 |
| WOCS 11028b | 0.916 | 14.871 | 0.150 | 0.909 ± 0.004 | 0.904 ± 0.015 |

**Table 3.** The eclipsing binary results from Sandquist et al. (2021). *BP-RP and G are from their main sequence fit in Gaia DR2 magnitudes and have been dereddened and corrected for extinction using $A_V$ from dust maps.

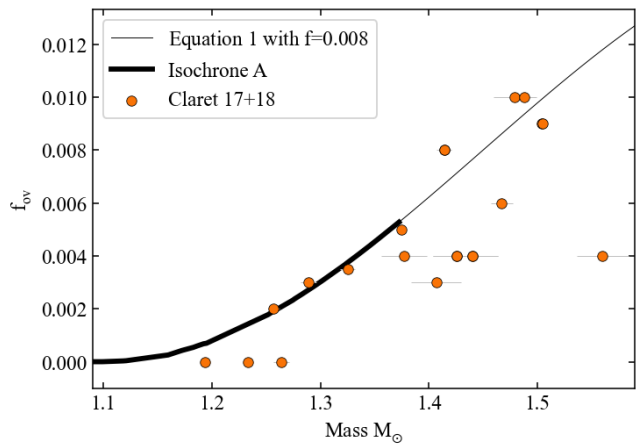


**Figure 6.** Comparing our mass-dependent overshoot used in Isochrone A with independent modelling of eclipsing binaries (Claret & Torres 2017, 2018). The dark section of the curve indicates the mass range along Isochrone A.

Isochrone EB are close to 0.5 $M_\odot$ larger than Isochrone A's at any given point in the colour-magnitude or $\log(g)$-$T_{\rm eff}$ diagrams. However, the $\alpha_{\rm MLT}$ values we applied to stellar models of different masses are not based on any known physics but are solely adapted by eye to fit the CMD diagram. From all the above, we conclude that even though Isochrone EB matches the mass and magnitude of WOCS11028a, the isochrone is unlikely to be a good model for the cluster. Also, preliminary results indicate that the luminosities of the giants predicted by the alternative isochrone EB are in tension with asteroseismic observations (Reyes et al., in preparation).

### *3.6.2 Possible causes of the model-mass conflict*

In addition to potential remaining shortcomings in stellar modelling, possible explanations for the conflict with the eclipsing binary masses include non-standard evolution of at least one component of WOCS11028, or systematics in the estimations of the eclipsing binary parameters. However, the presence of lithium in the spectra of the binary makes it unlikely that these stars have interacted in the past or resulted from a merger event, as, in such scenarios, lithium would have been consumed by the original lower mass stars with deeper surface convection zones, before merging (Sandquist et al. 2021).

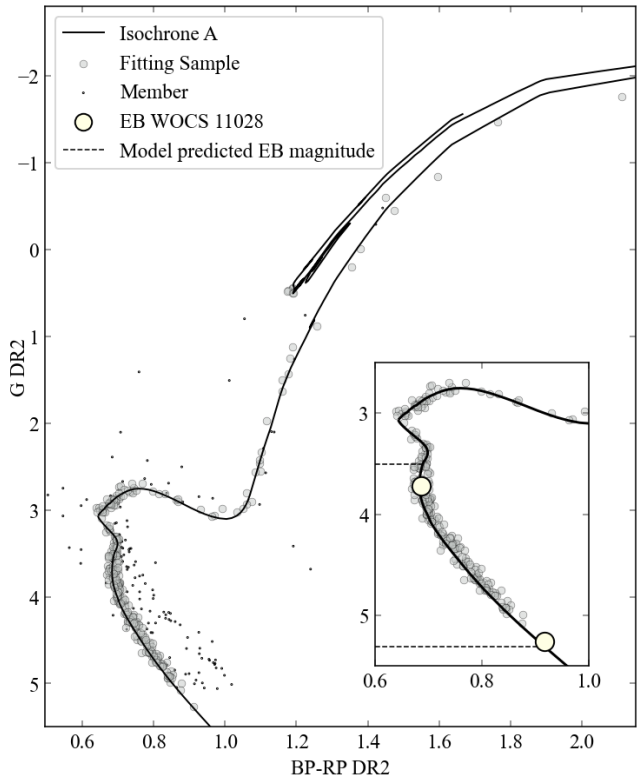


**Figure 7.** The de-reddened colour-magnitude diagram of our M67 sample and the 3.95 Gyr old best fitting isochrone from this work, Isochrone A. In small black symbols: stars with RUWE>1.2, stars in multiple star systems, and stellar products of non-standard evolution, as well as suspected binary members manually removed from the sample (end of Section 2.2). Several blue straggler members are bluer than 0.5 and are not shown in the figure. In grey symbols: presumed single members. Inset: the eclipsing binary system WOCS 11028 in large off-white circles resulting from the deconvolution of the binary's photometry, see Table 3. Dashed lines show the isochrone's predicted magnitudes for the masses of the two binary components. $\Delta G_{\rm mag}$ is $-0.05 \pm 0.09$, or $-0.67\sigma$ for the secondary component and $+0.21 \pm 0.06$, or $+12\sigma$ for the primary component, where $\sigma$ values correspond to those shown in Table 3.

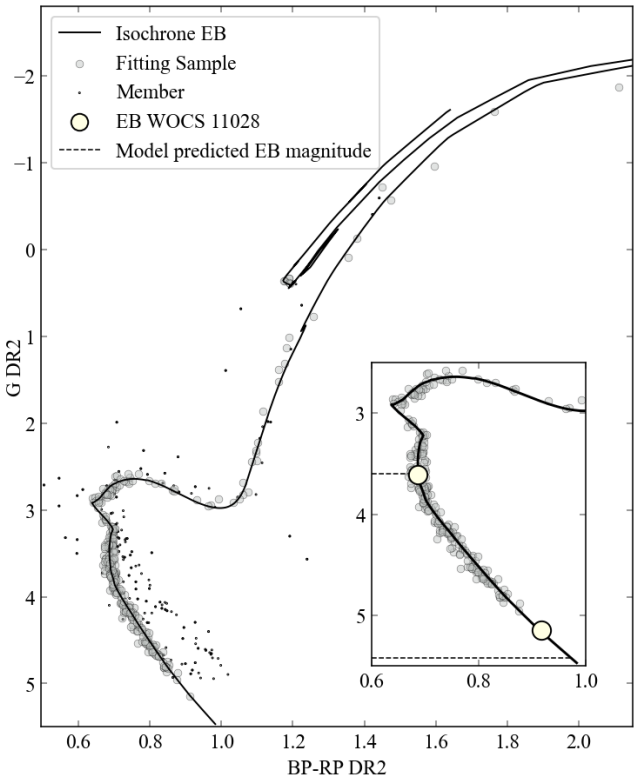


**Figure 8.** Alternative Isochrone EB. Dashed lines in the inset show predicted magnitudes for the masses of the two binary components. $\Delta G_{\rm mag}$ is $0.01 \pm 0.06$ ($0.3\sigma$) for the primary component and $-0.27 \pm 0.09$, or $-4\sigma$ for the secondary component, where $\sigma$ values correspond to those shown in Table 3. Symbols follow Figure7.

Possible grounds for an altered eclipsing binary mass or luminosity would be the non-detected presence of a third star in the WOCS 11028 system. Such has been the case in the past in the young Hyades open cluster and the multiple system HD27130 where a previous mass overestimate due to an unseen third component led Lebreton et al. (2001) to estimate a helium content of $Y = 0.255$, while more recent studies indicate a higher than solar helium abundance for the Hyades (see Brandner et al. 2023, and references therein). For a discussion on the effects of HD27130 on the derived properties of the Hyades see Brogaard et al. (2021). However, even if there were a faint third star hiding in the photometry of WOCS11028 due to a particularly pathological setup of the multiple system, it would mean a similar and small mass shift to both known components, with no significant change in their relative positions in the colour-magnitude diagram. This opens up the possibility that models do not accurately represent the speed at which stars evolve during the main sequence, at least for stars around $1.2 M_\odot$, which could make us reconsider our understanding of stellar evolution. In summary, the case of WOCS11028 is still very much open and requires further investigation.

| Parameter | Isochrone EB |
|---|---|
| Age | 3.55 Gyrs |
| Distance modulus | 9.73 |
| Nuclear reaction network | h1, he3, he4, c12, n14, o16, ne20, mg24 (MESA's basic.net) |
| Solar mixture | GS98 (Grevesse & Sauval 1998) |
| Z | 0.0196 |
| Y | 0.2710 |
| $\Delta Z/\Delta Y$ | 1.18 |
| EoS | HELM (Timmes & Swesty 2000) + Skye (Jermyn et al. 2021) + FreeEOS (Irwin 2004) + OPAL (Rogers & Nayfonov 2002) + SCVH (Saumon et al. 1995) |
| Interior opacities | OPAL (Iglesias & Rogers 1993, 1996) |
| Low temperature opacities | FA05 (Ferguson et al. 2005) |
| Atmospheres | $T(\tau)$, varying, Eddington |
| Overshooting | Exponential, increasing with mass, sharp increase at M=1.32$M_\odot$ |
| $\alpha_{\rm MLT}$ | Variable, adjusted manually |
| MLT_option | Henyey |
| Mass loss | No mass loss |
| Convection | Schwarzschild criterion |
| Diffusion | Yes |

**Table 4.** Summary of parameters in MESA models for Isochrone EB shown in Figure8.

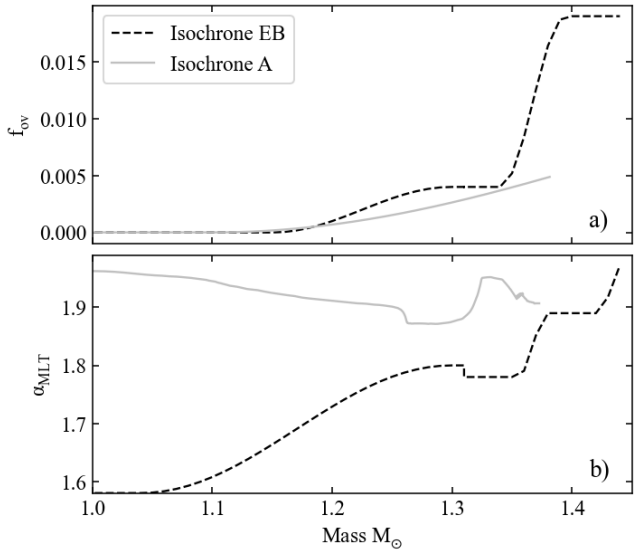


**Figure 9.** (a) The overshooting parameter $f_{ov}$ and the mixing length parameter $\alpha_{MLT}$ used in Isochrone EB (dashed) shown along the values used in Isochrone A (solid grey).

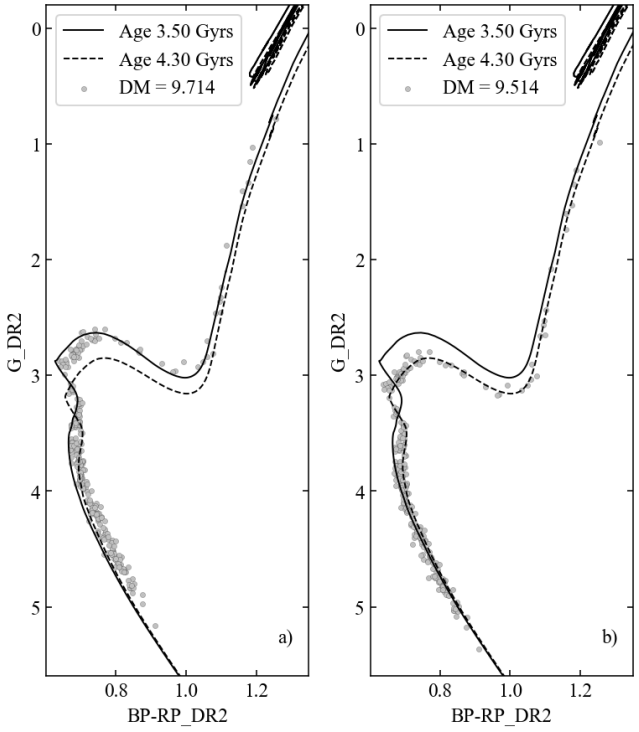


**Figure 10.** Isochrones of 3.50 Gyrs (solid) and 4.3 Gyrs (dashed) using the same physics as Isochrone A. (a) M67 isochrone fitting sample with a distance modulus is 9.714. (b) same as panel a, but for a distance modulus of 9.514.

## 4 AGE UNCERTAINTY THROUGH CHI-SQUARE ANALYSIS

Although we followed the traditional qualitative approach of matching the input physics of Isochrone A to the M67 colour-magnitude diagram, we will in the following look to estimate the age uncertainty using a $\chi^2$ approach. We take our isochrone-fitting sample from section 2.2 and further remove the stars that have evolved beyond the point where the red giant branch leaves the $\log(g)$-$T_{\rm eff}$ area covered by the 3D grid, marked by the segmented line in Figure 5b.

We vary the model age between 3.5 and 4.3 Gyrs, covering the age range quoted in literature (VandenBerg & Stetson 2004; Sarajedini et al. 2009; Barnes et al. 2016), and the distance modulus within $2\sigma$ of our Gaia DR3 parallax-derived value of $9.614 \pm 0.049$. Figure 10 shows the extremes of varying age and distance modulus like this.

For each combination of age and distance modulus, we used the nearest matching point on the isochrone as the expected value ($\vec{x}_{{\rm exp},i}$) for each star ($\vec{x}_{{\rm obs},i}$) in a $\chi^2$-like goodness of fit analysis. Following Sandquist et al. (2021), we define a $\chi^2$-like parameter involving fractional colour and magnitude differences, of the form:

$$\frac{1}{N}\sum_{i=0}^{N}\frac{(\vec{x}_{{\rm obs},i}-\vec{x}_{{\rm exp},i})^2}{\vec{x}^2_{{\rm exp},i}}, \quad \vec{x}=({\rm col}_i, {\rm mag}_i) \tag{2}$$

that we later rescale so that the lowest $\chi^2$ value equals 1. We do not include a $\sigma$ in this expression because Gaia does not provide magnitude uncertainties. Figure 11 shows the age versus distance modulus space colour-coded by this (rescaled) parameter. Figure 11a presents the combined statistics of both main-sequence and giant stars, which we will use in the following analysis. We find that the lowest $\chi^2$ (black triangle) is at a distance modulus about $1\sigma$ below the parallax-based value (black circle), and with a corresponding age of 4.04 Gyrs. If this were to be caused by any systematics in Gaia DR3 parallaxes, it would correspond to about 25 $\mu$as. However, there is no indication that such systematics exist beyond the Lindegren et al. (2021) corrections (Zinn 2021), which we have already included. Furthermore, a smaller distance modulus would increase discrepancies between models and WOCS 11028. We, therefore, prefer to quote the age as 3.95 Gyrs –the black circle in Figure 11a – and our confidence interval as [3.80, 4.11] Gyrs, the point where the $\chi^2$ has risen by 1 from its minimum value along the adopted parallax-based distance modulus (black error bars). For completeness, we also present the $\chi^2$ results restricted to main sequence stars in Figure 11b, and giants in Figure 11c, where the split into those groups is defined by core hydrogen exhaustion (the hottest point along the isochrone). For reference, we copy in the latter panels with grey symbols the location of the lowest $\chi^2$ points from panel a.

## 5 CONCLUSIONS AND FUTURE WORK

We have presented a detailed isochrone, Isochrone A, specifically designed for the low-reddening cluster M67 using state-of-the-art stellar input physics. Our models match the morphology of the tight cluster sequence better than previously reported in the literature in Gaia colours and magnitudes. Our results indicate that adopting a mixing length $\alpha_{\rm MLT}$ that is dependent on $T_{\rm eff}$ and $\log(g)$, such as the one obtained from the 3D-grid, can improve the fit of models to observations. Therefore, this approach should be considered in future standard stellar models. Our best age estimate is $3.95^{+0.16}_{-0.15}$ Gyrs, in agreement with the estimates from VandenBerg & Stetson (2004) ($4.0 \pm 0.4$ Gyrs from *BV* photometry), Sarajedini et al. (2009) (3.5 – 4.0 Gyrs from 2MASS photometry), (Barnes et al. 2016) ($4.2 \pm 0.2$ Gyrs from gyrochronology), Bressan et al. (2012) (3.7 Gyrs from *BV* photometry using PARSEC isochrones v1.2), and Nguyen et al. (2022) (3.9 Gyrs from Gaia DR2 photometry using PARSEC isochrones v2.0).

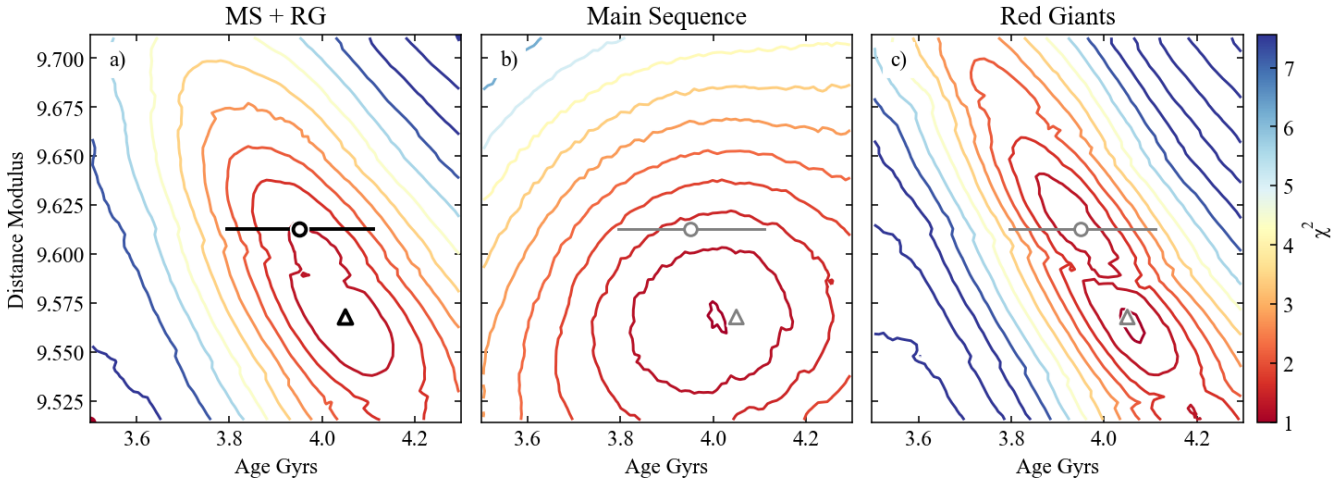


**Figure 11.** $\chi^2$-like statistics from M67 main sequence and giant stars for isochrone ages between 3.5 and 4.3 Gyrs and distance modulus within $2\sigma$ of our Gaia parallax-derived value of 9.614 ± 0.049. The triangle shows the overall lowest $\chi^2$ for panel a, and the circle, including errorbars, shows our quoted age of $3.95^{+0.16}_{-0.15}$ Gyrs, corresponding to the lowest $\chi^2$ at distance modulus = 9.614. The position of the circle and the triangle are copied in the other panels for completeness.

Despite the improvements in the match to the cluster colour-magnitude diagram, our isochrone shows some disagreement with the measured mass for the primary component of the eclipsing binary WOCS11028 near the cluster turnoff. The only alternative isochrone we could anchor on the primary eclipsing binary is based on improbable input physics and fundamental cluster properties. Therefore, we conclude that the literature values of the masses and luminosities for the eclipsing binary system are incompatible with the rest of the cluster in a scenario where both binary components have evolved independently. Of course, this is under the perhaps unrealistic assumption that there are no shortcomings in our current model input physics.

To help resolve the issues surrounding WOCS 11028, one could potentially use detailed asteroseismic modelling to confirm masses and radii of the cluster stars. In addition, high-resolution imaging of the binary might be able to detect any undiscovered component that could affect the mass and radius estimates.

## SOFTWARE

Extinction correction performed using the *dustmaps* python tool (Green 2018). https://dustmaps.readthedocs.io/en/latest/

Interpolation to bolometric correction tables was performed using the python package *isochrones* v2.1 (Morton 2015). https://isochrones.readthedocs.io/en/latest/

Isochrones are constructed using the fortran code *iso* described in Dotter (2016a,b). https://cmasher.readthedocs.io/user/introduction.html

## ACKNOWLEDGEMENTS

D.S. is supported by the Australian Research Council (DP190100666). This work has made use of data from the European Space Agency (ESA) mission *Gaia* (https://www.cosmos.esa.int/Gaia), processed by the *Gaia* Data Processing and Analysis Consortium (DPAC, https://www.cosmos.esa.int/web/Gaia/dpac/consortium). Funding for the DPAC has been provided by national institutions, in particular the institutions participating in the *Gaia* Multilateral Agreement.

This research includes computations using the computational cluster Katana supported by Research Technology Services at UNSW Sydney, https://doi.org/10.26190/669x-a286.

We would like to thank the participants of the MIAPbP Program "Stellar Astrophysics" in Garching August 2023 for the discussion on artificial metallicity trends with $\log(g)$ when not using 3D-NLTE spectroscopic analyses.

## DATA AVAILABILITY

The Isochrone and the inlists for the models presented in this work can be found on the Zenodo online software platform, https://zenodo.org/records/12616441.

## APPENDIX A: ISOCHRONE A

Our final 3.95 Gyr isochrone, Isochrone A, is partially presented in Table A1, and the full isochrone from main sequence to core helium burning is available for download through the online version of the paper. The column names correspond to standard MESA parameters, except mixing_length_alpha and f_overshoot, which correspond to $\alpha_{\rm MLT}$ and $f_{\rm ov}$, respectively, as denoted in the text.

## APPENDIX B: OTHER ISOCHRONES

Figure B1 shows isochrones from two recent works that have been fitted to the M67 colour-magnitude diagram in Gaia colours. These are models designed for general use and, therefore, not specifically for M67. Nguyen et al. (2022) use The PAdova and tRieste Stellar Evolutionary Code v2.0, and similarly to Isochrone A from this work, incorporates a mass-dependent overshoot and the AESOPUS

| isochrone_age_yr | star_mass | log_L | log_Teff | log_R | log_g | ... | mixing_length_alpha | f_overshoot |
|---|---|---|---|---|---|---|---|---|
| 3.9500e9 | 0.8506 | -0.4003 | 3.7133 | -0.1038 | 4.5755 | ... | 1.9849 | 0.0000 |
| 3.9500e9 | 0.8591 | -0.3778 | 3.7165 | -0.0989 | 4.5700 | ... | 1.9774 | 0.0000 |
| 3.9500e9 | 0.8676 | -0.3557 | 3.7195 | -0.0940 | 4.5644 | ... | 1.9691 | 0.0000 |
| 3.9500e9 | 0.8759 | -0.3339 | 3.7226 | -0.0891 | 4.5587 | ... | 1.9637 | 0.0000 |
| 3.9500e9 | 0.8841 | -0.3127 | 3.7255 | -0.0843 | 4.5532 | ... | 1.9602 | 0.0000 |

**Table A1.** First few rows of selected columns of Isochrone A. The full isochrone, including key internal structure parameters and photometric bands, is available for download from the online version of the paper, or on Zenodo (See Data Availability.)

opacity tables. Their best fit to M67 is shown with our stellar fitting sample in Figure B1a. Choi et al. (2018) -the MIST models- use the MESA evolutionary code, and a fixed core overshoot $f_{ov} = 0.016$. Figure B1b shows their fit to M67. In each panel, the fitting sample is corrected to absolute magnitudes using the distance modulus adopted by the corresponding authors.

Figure B2 shows the qualitative effects of our atmosphere and core-overshoot choices from sections 3.2 and 3.5.2 in our models. In all panels, Isochrone A is shown in green and: Panel (a) shows a base-model from where we start: similar to the MIST models, but with our chosen initial composition (2.2.5), age, and the carefully chosen (fixed) values of overshoot $f_{ov}$ and $\alpha_{MLT}$ to best fit M67; Column (a) in the table just below the figure indicates five key parameter values. We see that the simplified model can still be made to fit the red giant branch well with $\alpha_{MLT}$=1.91, but the model is too hot compared with the main-sequence. In (b) we show the base model from (a), but now applying the 3D-grid-based varying $\alpha_{MLT}$ and associated atmospheric improvements from Trampedach et al. (2014a,b) (see column (b) in table). These changes move the isochrone towards colder temperatures, making the model fit the main sequence and subgiants better, however the red giant branch is now "too cold", at least with the age and [Fe/H] of Isochrone A. In (c) we now also add low opacity tables that account for CNO processes in red giants (see column (c)). This brings the model back into agreement with the red giants. The only remaining simplified parameter in (c) is the fixed overshoot $f_{ov}$, which has a subtle, but noticeable, effect on the morphology of the main sequence turnoff, where the even smaller values of $f_{ov}$ used in Isochrone A at these masses (Figure 5c, d) appear to fit the stellar sequence marginally better.

## APPENDIX C: EXTINCTION MAPS

We present extinction maps of the region around the M67 cluster, centred at RA = 215.69°, Dec = +31.92° (galactic coordinates), that we considered for differential de-reddening of M67 photometry, aiming to reduce the scatter of the cluster sequence in the colour-magnitude diagram. We compared the 2D extinction map by Planck Collaboration et al. (2016) with the Bayestar 3D reddening map (Green et al. 2019) and used the coefficients from Table 6 from Schlafly & Finkbeiner (2011) to convert from Bayestar reddening to $A_V$ extinctions. We found that the 2D map results in a smoother map of extinctions that works well to reduce the scatter in the M67 colour-magnitude diagram (Figure 3), while the 3D Bayestar map does not behave well, at least in this area of the sky, and at the small scales we require. The 3D extinction map looks pixelated and shows sharp variations, as seen in Figure C1. This could be related to the systematic trends in reddening identified by Green et al. (2019) at low reddenings. This is a note of caution for future cluster studies.

## APPENDIX D: METALLICITY TREND IN RED GIANTS FROM APOGEE DR17

The trend of decreasing metallicity with decreasing $\log(g)$ observed in M67 was observed in almost all of the clusters included in the APOGREE DR17 Open Cluster Chemical Abundances and Mapping Catalogue [7]. In Figure D1 we show the clusters in the catalogue with more than 80 members, and fit the metallicity trend for $\log(g) < 3.0$ in each cluster.

## REFERENCES


Alam S., et al., 2015, ApJS, 219, 12
Asplund M., Grevesse N., Guedel M., Sauval A. J., 2005, arXiv e-prints, pp astro–ph/0510377
Asplund M., Grevesse N., Sauval A. J., Scott P., 2009, ARA&A, 47, 481
Ball W. H., 2021, Research Notes of the American Astronomical Society, 5, 7
Barker H., Paust N. E. Q., 2018, PASP, 130, 034204
Barnes S. A., Weingrill J., Fritzewski D., Strassmeier K. G., Platais I., 2016, ApJ, 823, 16
Beeson K. L., et al., 2024, MNRAS, 529, 2483
Bertelli Motta C., et al., 2018, MNRAS, 478, 425
Brandner W., Calissendorff P., Kopytova T., 2023, MNRAS, 518, 662
Bressan A., Marigo P., Girardi L., Salasnich B., Dal Cero C., Rubele S., Nanni A., 2012, MNRAS, 427, 127
Brogaard K., et al., 2012, A&A, 543, A106
Brogaard K., et al., 2021, A&A, 645, A25
Buder S., et al., 2021, MNRAS, 506, 150
Choi J., Dotter A., Conroy C., Cantiello M., Paxton B., Johnson B. D., 2016, ApJ, 823, 102
Choi J., Conroy C., Ting Y.-S., Cargile P. A., Dotter A., Johnson B. D., 2018, ApJ, 863, 65
Claret A., Torres G., 2017, ApJ, 849, 18
Claret A., Torres G., 2018, ApJ, 859, 100
Constantino T., Baraffe I., 2018, A&A, 618, A177
Danielski C., Babusiaux C., Ruiz-Dern L., Sartoretti P., Arenou F., 2018, A&A, 614, A19
Dotter A., 2016a, ISO: Isochrone construction, Astrophysics Source Code Library, record ascl:1601.021 (ascl:1601.021)
Dotter A., 2016b, ApJS, 222, 8
Ferguson J. W., Alexander D. R., Allard F., Barman T., Bodnarik J. G., Hauschildt P. H., Heffner-Wong A., Tamanai A., 2005, ApJ, 623, 585
Gaia Collaboration 2022, VizieR Online Data Catalog, p. I/355
Gaia Collaboration et al., 2016, A&A, 595, A1
Gaia Collaboration et al., 2018a, A&A, 616, A1
Gaia Collaboration et al., 2018b, A&A, 616, A10
Gaia Collaboration et al., 2021, A&A, 649, A1
Gaia Collaboration et al., 2022, arXiv e-prints, p. arXiv:2206.05595
Geller A. M., Latham D. W., Mathieu R. D., 2015, AJ, 150, 97


[7] https://www.sdss4.org/dr17/data_access/value-added-catalogs/?vac_id=open-cluster-chemical-abundances-and-mapping-catalog

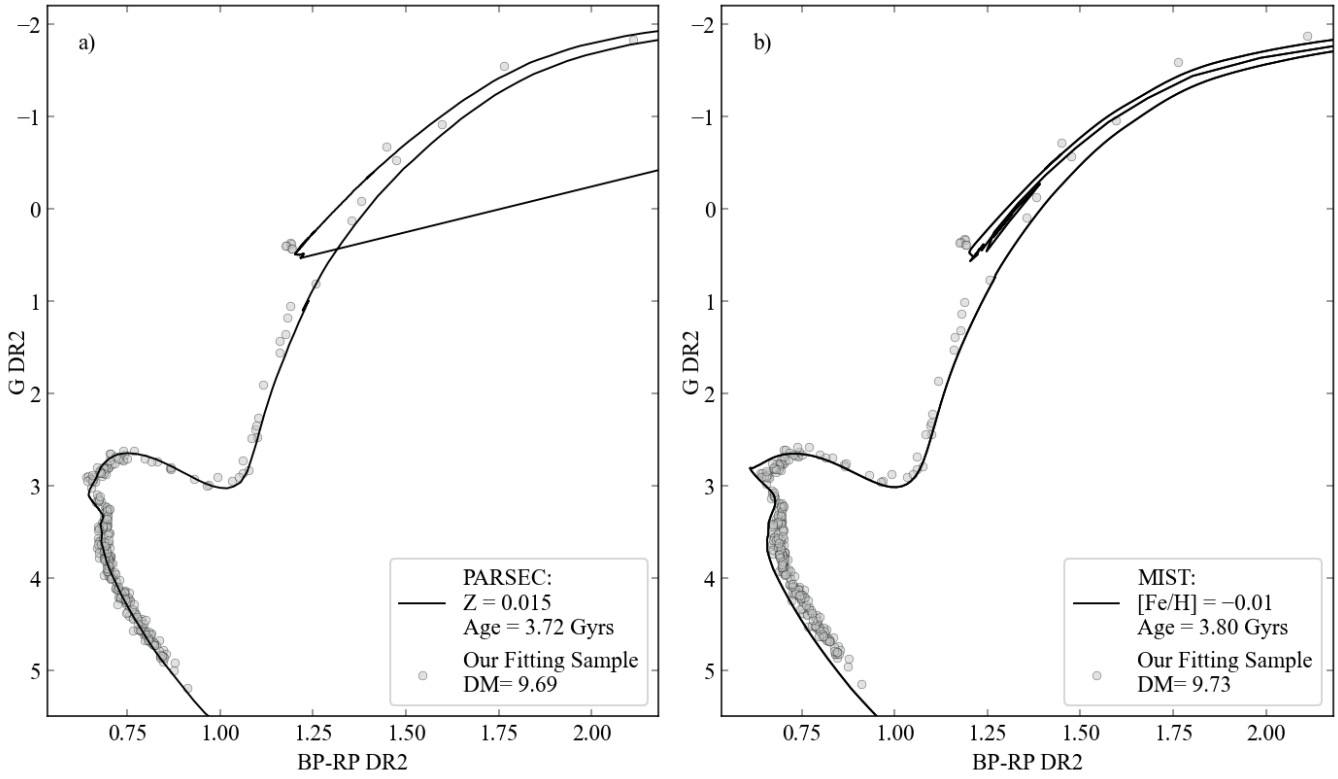


**Figure B1.** Best fit isochrones to the M67 Gaia colour magnitude diagram from a) Nguyen et al. (2022), and b) Choi et al. (2018).


Geller A. M., Mathieu R. D., Latham D. W., Pollack M., Torres G., Leiner E. M., 2021, AJ, 161, 190
Gilliland R. L., et al., 1993, AJ, 106, 2441
Green G., 2018, The Journal of Open Source Software, 3, 695
Green G. M., Schlafly E., Zucker C., Speagle J. S., Finkbeiner D., 2019, ApJ, 887, 93
Grevesse N., Sauval A. J., 1998, Space Sci. Rev., 85, 161
Herwig F., 2000, A&A, 360, 952
Holtzman J. A., et al., 2018, AJ, 156, 125
Huber D., Bryson S. T., et al. 2017, VizieR Online Data Catalog, p. IV/34
Iglesias C. A., Rogers F. J., 1993, ApJ, 412, 752
Iglesias C. A., Rogers F. J., 1996, ApJ, 464, 943
Irwin A. W., 2004, The FreeEOS Code for Calculating the Equation of State for Stellar Interiors, http://freeeos.sourceforge.net/
Jermyn A. S., Schwab J., Bauer E., Timmes F. X., Potekhin A. Y., 2021, ApJ, 913, 72
Jermyn A. S., et al., 2023, ApJS, 265, 15
Joyce M., Tayar J., 2023, Galaxies, 11, 75
Karakas A. I., 2017, Low- and Intermediate-Mass Stars. Springer International Publishing, Cham, pp 1–21, doi:10.1007/978-3-319-20794-0_117-1, https://doi.org/10.1007/978-3-319-20794-0_117-1
Khan S., et al., 2019, A&A, 628, A35
Kippenhahn R., Weigert A., Weiss A., 2013, Stellar Structure and Evolution, doi:10.1007/978-3-642-30304-3.
Lebreton Y., Fernandes J., Lejeune T., 2001, A&A, 374, 540
Leiner E., Mathieu R. D., Vanderburg A., Gosnell N. M., Smith J. C., 2019, ApJ, 881, 47
Li G., et al., 2023, arXiv e-prints, p. arXiv:2311.16991
Li T., Bi S., Davies G. R., Bedding T. R., Li Y., Stello D., Reyes C., 2024, MNRAS, 530, 2810
Lindegren L., et al., 2018, A&A, 616, A2
Lindegren L., et al., 2021, A&A, 649, A4
Lindsay C. J., Ong J. M. J., Basu S., 2024, arXiv e-prints, p. arXiv:2402.12461
Liu F., Asplund M., Yong D., Feltzing S., Dotter A., Meléndez J., Ramírez I., 2019, A&A, 627, A117
Magic Z., Serenelli A., Weiss A., Chaboyer B., 2010, ApJ, 718, 1378
Marigo P., Aringer B., 2009, A&A, 508, 1539
Mathieu R. D., Latham D. W., 1986, AJ, 92, 1364
Mathieu R. D., van den Berg M., Torres G., Latham D., Verbunt F., Stassun K., 2003, AJ, 125, 246
Mathys G., 1991, A&A, 245, 467
Miglio A., et al., 2012, MNRAS, 419, 2077
Montgomery K. A., Marschall L. A., Janes K. A., 1993, AJ, 106, 181
Morton T. D., 2015, isochrones: Stellar model grid package, Astrophysics Source Code Library, record ascl:1503.010 (ascl:1503.010)
Mosumgaard J. R., Ball W. H., Silva Aguirre V., Weiss A., Christensen-Dalsgaard J., 2018, MNRAS, 478, 5650
Nguyen C. T., et al., 2022, A&A, 665, A126
Nissen P. E., Twarog B. A., Crawford D. L., 1987, AJ, 93, 634
Paxton B., Bildsten L., Dotter A., Herwig F., Lesaffre P., Timmes F., 2011, ApJS, 192, 3
Paxton B., et al., 2013, ApJS, 208, 4
Paxton B., et al., 2015, ApJS, 220, 15
Paxton B., et al., 2018, ApJS, 234, 34
Paxton B., et al., 2019, ApJS, 243, 10
Pinsonneault M. H., Terndrup D. M., Hanson R. B., Stauffer J. R., 2004, ApJ, 600, 946
Planck Collaboration et al., 2016, A&A, 594, A13
Reimers D., 1975, in , Problems in stellar atmospheres and envelopes.. Springer-Verlag, pp 229–256
Rogers F. J., Nayfonov A., 2002, ApJ, 576, 1064
Roxburgh I. W., 1992, A&A, 266, 291
Salaris M., Cassisi S., 2017, Royal Society Open Science, 4, 170192
Sanders W. L., 1977, A&AS, 27, 89
Sandquist E. L., 2004, MNRAS, 347, 101
Sandquist E. L., et al., 2016, ApJ, 831, 11

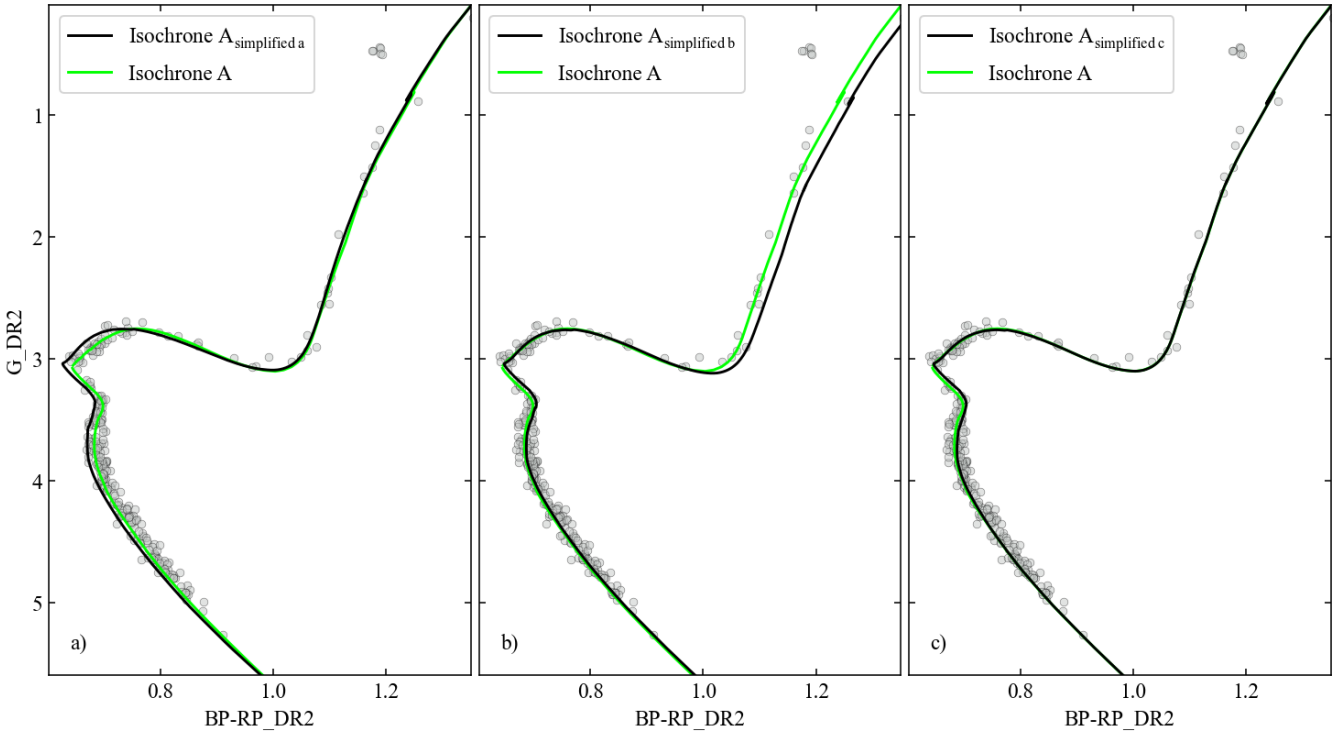


| **Parameter** | **(a)** | **(b)** | **(c)** | **Isochrone A** |
|---|---|---|---|---|
| $\alpha_{\rm MLT}$ | 1.91 | 3D grid | 3D grid | 3D grid |
| $\mathbf{T}(\tau)$ | Eddington | Trampedach solar | Trampedach solar | Trampedach solar |
| **photospheric transition** | default | improved | improved | improved |
| **low T opacities** | FA05 | FA05 | AESOPUS | AESOPUS |
| **core overshoot** | fixed $f_{\rm ov=0.004}$ | fixed $f_{\rm ov=0.004}$ | fixed $f_{\rm ov=0.004}$ | mass-dependent |

**Figure B2.** In b) and c), the isochrones in black show the effects of cumulatively applying parameter 'improvements' to the simplified form of Isochrone A shown in (a). The table below the figure shows the model parameters we vary and their values, along with the values used in Isochrone A.


Sandquist E. L., et al., 2021, AJ, 161, 59
Sarajedini A., Dotter A., Kirkpatrick A., 2009, ApJ, 698, 1872
Saumon D., Chabrier G., van Horn H. M., 1995, ApJS, 99, 713
Schlafly E. F., Finkbeiner D. P., 2011, The Astrophysical Journal, 737, 103
Schlegel D. J., Finkbeiner D. P., Davis M., 1998, ApJ, 500, 525
Schönrich R., McMillan P., Eyer L., 2019, MNRAS, 487, 3568
Song N., Alexeeva S., Sitnova T., Wang L., Grupp F., Zhao G., 2020, A&A, 635, A176
Souto D., et al., 2018, ApJ, 857, 14
Souto D., et al., 2019, ApJ, 874, 97
Spoo T., et al., 2022, AJ, 163, 229
Stassun K. G., Torres G., 2018, ApJ, 862, 61
Stassun K. G., et al., 2019, AJ, 158, 138
Stello D., et al., 2006, MNRAS, 373, 1141
Stello D., et al., 2016, ApJ, 832, 133
Strom S. E., Strom K. M., Bregman J. N., 1971, PASP, 83, 768
Taylor B. J., 2007, AJ, 133, 370
Timmes F. X., Swesty F. D., 2000, ApJS, 126, 501
Trampedach R., Stein R. F., Christensen-Dalsgaard J., Nordlund Å., Asplund M., 2014a, MNRAS, 442, 805
Trampedach R., Stein R. F., Christensen-Dalsgaard J., Nordlund Å., Asplund M., 2014b, MNRAS, 445, 4366
VandenBerg D. A., Stetson P. B., 2004, PASP, 116, 997
VandenBerg D. A., Bergbusch P. A., Dowler P. D., 2006, ApJS, 162, 375
VandenBerg D. A., Gustafsson B., Edvardsson B., Eriksson K., Ferguson J., 2007, ApJ, 666, L105
Viani L. S., Basu S., 2020, ApJ, 904, 22
Yadav R. K. S., et al., 2008, A&A, 484, 609
Zinn J. C., 2021, AJ, 161, 214
Zinn J. C., Pinsonneault M. H., Huber D., Stello D., 2019, ApJ, 878, 136


This paper has been typeset from a TEX/LATEX file prepared by the author.

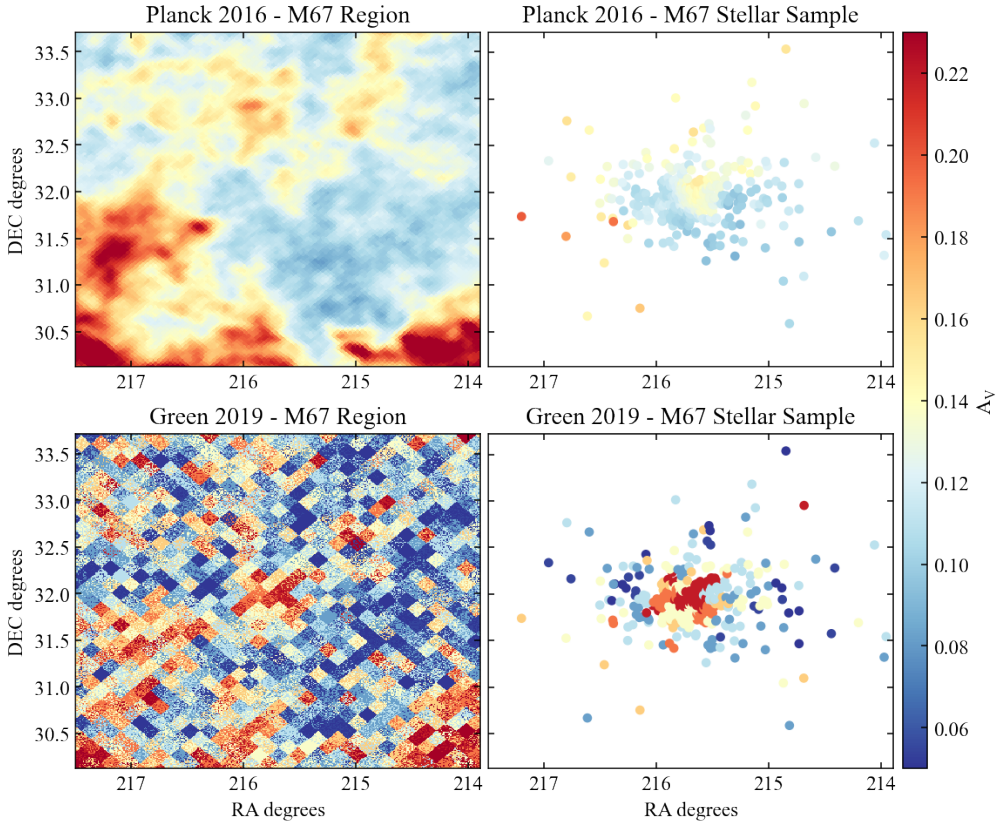


**Figure C1.** Extinction maps in galactic coordinates of the M67 cluster region (left) and of our M67 stellar sample (right). The colour expresses the extinction $A_V$ at each point of the sky.

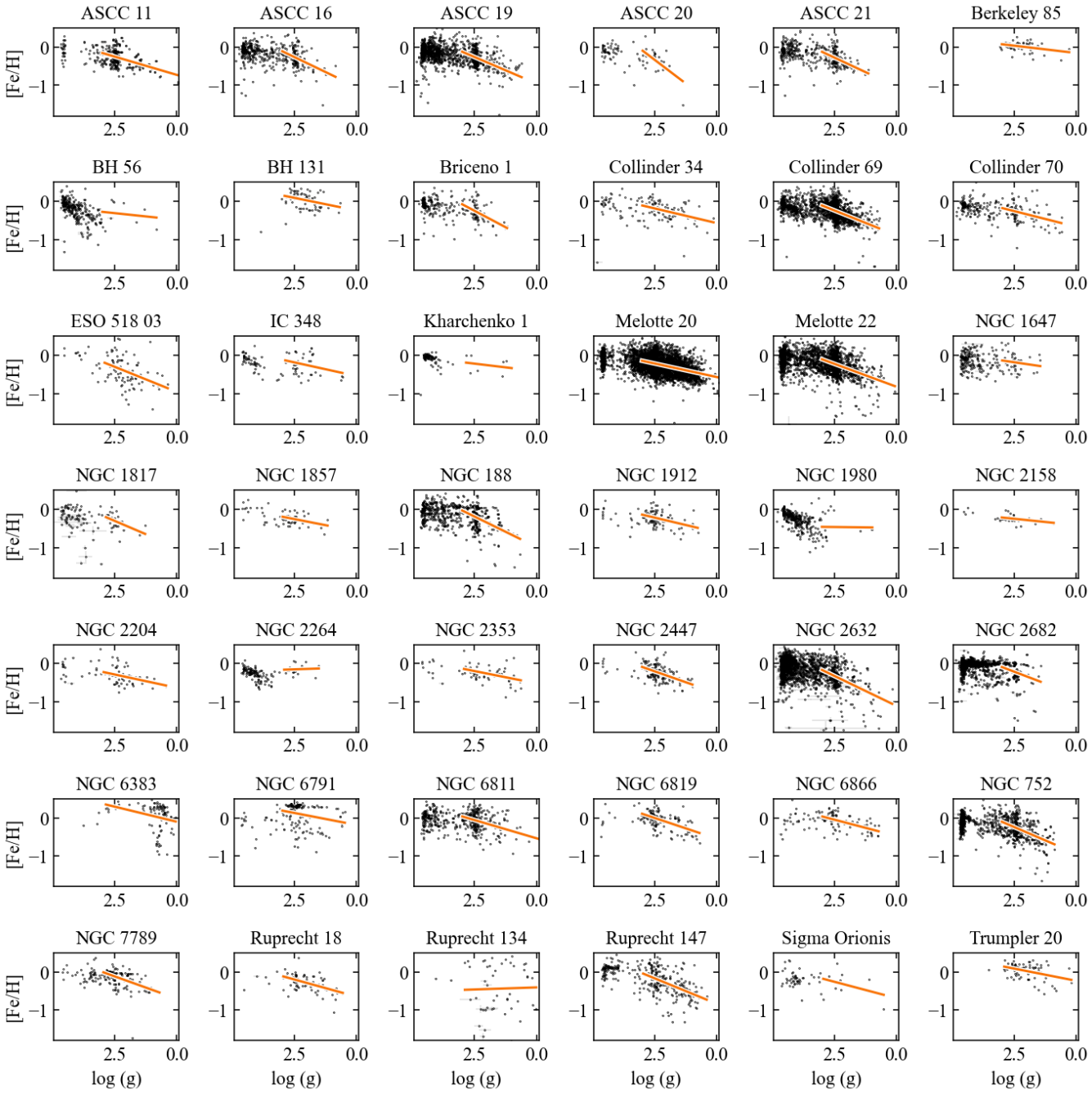


**Figure D1.** Clusters from the APOGEE DR17 Open Cluster Chemical Abundances and Mapping Catalogue with more than 80 cluster members (alphabetically ordered). The orange lines show a fit to the metallicities of all stars with $\log(g)$<= 3.0 within each cluster.